

The role of solute diffusion in the dynamical evolution of directional solidification: From a viewpoint of dissipation

Fengyi Yu

CAS Key Laboratory of Mechanical Behavior and Design of Materials, Department of Modern Mechanics,
University of Science and Technology of China, Hefei 230026, China

E-mail address: fengyi.yu.90@gmail.com

Abstract

To control the properties of as-solidified components, it is essential to link the technological parameters and structures accurately enough, requiring deep understand of solidification dynamics. The existing theoretical insights mostly focus on one single dendrite tip, ignoring the interfacial effects of the neighboring ones and the continuity of evolution. Since solidification patterns are dissipative structures formed out of equilibrium in an open system, the investigation during the entire process and the insights from dissipation could give a deeper understanding of solidification dynamics. In this paper, through the quantitative phase-field model, the dynamic evolution of directional solidification is investigated. Firstly, the evolution of the characteristic parameters with time is discussed in detail, demonstrating the dissipative features of solidification. Secondly, by adjusting the solute diffusion coefficient D_L , the dissipation due to an undercooling of the interface can be altered. With different D_L , the dynamic evolution in the directional solidification is discussed, including the planar growth and instability, the dendrite growth, and the steady-state growth. The role of solute diffusion in solidification evolution from the viewpoint of dissipation is given out. The investigations illustrate the dynamic evolution of interfaces does not has unique relationships with the characteristic parameters, such as V_I , c_0 , ρ , and R_{tip} , etc. Because solidification patterns are dissipative structures formed out of equilibrium. The degree of dissipation and non-equilibrium of the system plays an important role during the evolution, which should be considered in the study.

Keywords

Solute diffusion; Directional solidification; Dissipation; Phase-field method.

1. Introduction

Solidification structures directly determines the properties of the as-solidified components, as well as their behaviors in subsequent forming processes. In controlling the properties of components better, it is essential to link technological parameters and solidification structures accurately enough, requiring deep understand of solidification dynamics. The competition between the transport processes of heat and mass and inherent length scale of material, induced by interface energy, determines the solidification dynamics [1,2]. In this spirit, considerable achievements have been made in recent years [3-23], including theoretical and numerical results, as well as the corresponding experimental observations.

Due to the complexity of solidification, researchers developed various theoretical models to describe the evolution at different stages, separately. For early stage growth, including the planar growth and instability, the descriptions go through the Constitutional Supercooling (CS) theory [9], Mullins-Sekerka (MS) analysis [10,11] to the Warren-Langer (WL) [12] model. The incubation time and average wavelength of the instability predicted by the theoretical model agree well with the experimental observations [13,14]. After the planar instability, solidification turns into dendrite growth (with or without sidebranches). Due to the different features, two stages should be distinguished in dendrite growth. The first is unsteady growth, velocity and shape of dendrite tip vary with time, and the second is steady-state growth, velocity and shape are constant [15]. The dynamics of dendrite growth is determined by competitive influences of the interface curvature ρ and velocity V . The influences can be regarded as two tip conditions. The first tip condition measures the strength of the mass flux feeding the growth of the tip region on the scale of diffusion length, which can be derived that expresses the product ρV^2 [16,17]. The second tip condition, fixes $\rho^2 V$, can be derived by a self-consistent solution of the growth equations on the scale of the tip where interface energy become extremely important [15]. It can be expressed mathematically as a solvability condition, predicting $\rho^2 V$ is a function of the anisotropic strength [18,19]. Together, these two tip conditions fix $V(t)$ and $\rho(t)$ uniquely, which can be computed separately for both the unsteady growth and steady-state growth, consisting with the Ivantsov solution [20]. Up to now, a number of theoretical insights have been made, expressing the relationships between the morphological evolution and characteristic parameters, such as ρ , V , R_{tip} , etc. However, the solutions of the theoretical models can only apply under the simple conditions. The theoretical insights mostly focus on one single dendrite tip, ignoring the interfacial effects of the neighboring ones. The interaction between the dendrites plays an important role in solidification [21], which should be considered. Moreover,

the separate descriptions at different stages mean the loss of continuity of the evolution, which could hardly represent the history-dependence of solidification.

Differing from the theoretical models, the numerical models can be applied to the complex conditions, which could handle complicated interfacial morphologies and varying solidification parameters [6,22,23]. The numerical methods have the advantages of representing the interfacial effects and investigating interface evolution in the entire solidification process. As one of them, the Phase-Field (PF) method has solid physical foundations and high numerical accuracy [24-26]. Specifically, physics underlying the construction of the PF model includes the insights of thermodynamics and dynamics of the transport process, as well as the effects of anisotropy [27,28]. When solving the governing equations, using an additional scalar field to implicitly represent the interface by one of its level sets, the PF method avoids the shape error caused by tracking interface. It could capture the complex interfacial morphologies and characteristic parameters at the interface with high accuracy. With these significant advantages, the PF method has been increasingly applied for investigating solidification dynamics, including the planar to cellular transition [29,30], the selection of growth direction [31-33], the competitive growth [34,35], the columnar to equiaxed transition [36,37], and the sidebranching dynamics [38-40], etc. The consistencies with the experimental observations demonstrate the accuracy of the PF method. However, the separate investigations at different stages neglects the fact that solidification is a history-dependent process. The initial evolution can be deterministic for the subsequent evolution [12]. Moreover, through exchanging heat and mass with the environment, solidification structures are formed out of equilibrium in an open system, i.e., a dissipative system. Unlike equilibrium systems, the dissipative systems (non-equilibrium) develop patterns, structures, or behaviors that they do not have when first formed. The investigation during the entire process and the insights from dissipation could give a deeper understanding of solidification dynamics.

In this paper, via the quantitative PF model, the dynamic evolution during directional solidification is investigated. Firstly, the evolution of the characteristic parameters with time is discussed in detail, showing the dissipative features. Secondly, by adjusting the solute diffusion coefficient D_L , the dissipation due to an undercooling of the solid/liquid (S/L) interface can be altered. With different D_L , the dynamic evolution of the characteristic parameters and interfacial morphologies during the directional solidification is discussed, including the planar growth and instability, the dendrite growth, and the steady-state growth. The role of solute diffusion in solidification evolution from the viewpoint of dissipation is given out.

2. Models and methodology

2.1. Theoretical model

The theoretical model is based on the linear instability analysis under non-steady-state conditions, the detailed derivations can be found in the literatures [12,41,42]. The following are the key equations.

The time-dependent concentration field ahead of the interface c_0 , position of interface z_0 and diffusion length l can be expressed as [12]:

$$c_0(z_0, t) = \frac{2D_L c_\infty}{2D_L - V_I(1-k)l} \quad (1)$$

$$\frac{\partial z_0}{\partial t} = V_I - V_P(t) = \frac{2D_L(z_0 - z_\infty)}{l(1-k)z_0} - V_P(t) \quad (2)$$

$$\frac{\partial l}{\partial t} = \frac{4D_L(z_\infty - kz_0)}{l(1-k)z_0} - \frac{l}{z_0 - z_\infty} \frac{\partial z_0}{\partial t} \quad (3)$$

where D_L is the solute diffusion coefficient in the liquid, c_∞ is the average concentration, k is the solute partition coefficient, and V_I is the instantaneous velocity of the interface. V_P is the time-dependent pulling speed. z_∞ is the steady-state position of the planar interface with the relation of $z_\infty = -m \cdot c_\infty / G$, where G is the thermal gradient, and m is the slope of the liquidus line in the phase diagram.

Based on the time-dependent linear stability analysis and the assumption of an infinitesimal sinusoidal perturbation with spacing frequency ω , the increase rate of perturbation amplitude can be given by:

$$\sigma_\omega(t) = [dA_\omega(t)/dt] / A_\omega(t) \quad (4)$$

where $A_\omega(t)$ is the amplitude. Combining the interface position and diffusion length in equations (2)-(3), the dispersion relation of the perturbation under the transient conditions can be expressed by:

$$q_\omega \left\{ 1 + \frac{2[z_0(t) - z_\infty]}{l(t)} + \frac{\Gamma \omega^2}{G} \right\} = \frac{V_I(t) - V_P(t)}{D_l} + \frac{2[z_0(t) - z_\infty]}{l(t)} \cdot \left[\frac{V_I(t)}{D_l} + \frac{\sigma_\omega(t)}{V_I(t)} + \frac{1}{z_0(t)} + \frac{\Gamma \omega^2}{G \cdot z_0(t)} \right] \quad (5)$$

where q_ω is the inverse decay length of the concentration fluctuation at the interface along the z direction.

Based on equation (5), the time-dependent increase rate of the amplification rate $\sigma_\omega(t)$ can be obtained. Then according to the solution of equation (4), the time-dependent amplitude is given by:

$$A_\omega(t) = A_\omega(0) \exp \left[\int_{t_0}^t \sigma_\omega(t) dt \right] \quad (6)$$

where t_0 is the critical time when σ_ω changes from negative to positive. $A_\omega(0)$ refers to the initial amplitude of the infinitesimal fluctuation.

2.2. Phase-Field model

The following is a brief introduction of the quantitative PF model of alloy solidification [43-45].

Firstly, a scalar variable $\phi(\mathbf{r}, t)$ is introduced to identify the state of phase, where $\phi=+1$ reflects the solid, $\phi=-1$ reflects the liquid, and intermediate values of ϕ reflects the S/L interface. Since ϕ varies smoothly across the interface, the sharp interface becomes diffuse and the phases turn into a continuous field, i.e., phase field $\phi(\mathbf{r}, t)$. For alloy solidification, the solute field $c(\mathbf{r}, t)$ is represented by the supersaturation field $U(\mathbf{r}, t)$:

$$U = \frac{1}{1-k} \left(\frac{2kc/c_\infty}{1+k-(1-k)\cdot\phi} - 1 \right) \quad (7)$$

In directional solidification, the so-called ‘‘frozen temperature approximation’’ is adopted, expressed in [equation \(8\)](#), based on the following assumptions: (1) The latent heat is ignored, i.e., the temperature field is undisturbed by interfacial evolution. (2) There is no flow in the liquid, consistent with the assumption that the densities of the solid and liquid are equal [2]. It should be pointed out, this approximation is only for the heat transport process. The thermodynamic model for solidification evolution includes the latent heat.

$$T(z, t) = T_0 + G(t) \left(z - z_0 - \int V_p(t) dt \right) \quad (8)$$

Finally, the governing equations of the phase field and supersaturation field are given by [43-45]:

$$\begin{aligned} a_s^2(\hat{n}) \left[1 - (1-k) \frac{z - z_0 - \int V_p(t) dt}{l_T} \right] \frac{\partial \phi}{\partial t} = \\ \nabla \cdot \left[a_s^2(\hat{n}) \vec{\nabla} \phi \right] - \partial_x (a_s(\hat{n}) \cdot a_s'(\hat{n}) \cdot \partial_y \phi) + \partial_y (a_s(\hat{n}) \cdot a_s'(\hat{n}) \cdot \partial_x \phi) \\ + \phi(1-\phi^2) - \lambda(1-\phi^2)^2 \left[U + \frac{z - z_0 - \int V_p(t) dt}{l_T} \right] \end{aligned} \quad (9)$$

$$\left(\frac{1+k}{2} - \frac{1-k}{2} \phi \right) \frac{\partial U}{\partial t} = \nabla \cdot \left[D_L \cdot q(\phi) \cdot \vec{\nabla} U - \vec{j}_{at} \right] + \frac{1}{2} [1 + (1-k)U] \frac{\partial \phi}{\partial t} \quad (10)$$

where,

$$l_T = \frac{\Delta T_0}{G(t)} = \frac{|m|c_\infty(1-k)}{kG(t)} \quad (11)$$

$$a_s(\hat{n}) \equiv a_s(\theta + \theta_0) = 1 + \varepsilon_4 \cos 4(\theta + \theta_0) \quad (12)$$

$$q(\phi) = \frac{1-\phi}{2} \quad (13)$$

$$\vec{j}_{at} = -\frac{1}{2\sqrt{2}} [1 + (1-k)U] \frac{\partial \phi}{\partial t} \frac{\bar{\nabla} \phi}{|\bar{\nabla} \phi|} \quad (14)$$

In these equations, l_T means the thermal length, where m is the slope of the liquidus line in the phase diagram. $a_s(\hat{n})$ is the four-fold anisotropy function in a 2D system, where ε_4 is the anisotropy strength, θ is the angle between the normal direction of the interface and the z-axis, θ_0 is the intersection angle between the Preferred Crystallographic Orientations (PCO) of the crystal and the Thermal Gradient Direction (TGD) (here TGD is parallel to the z-axis). $q(\phi)$ is an interpolation function determining the varying solute diffusion coefficient across the domain. \vec{j}_{at} is the ATC term, where $\partial\phi/\partial t$ represents the rate of solidification, $\nabla\phi/|\nabla\phi|$ is the unit length along the normal direction of the S/L interface.

In performing quantitative simulations, it is essential to obtain the precise relationships between the calculation parameters in the equations and the real physical qualities. The asymptotic analysis can achieve this goal. Specifically, the perturbation analyses have been performed on each scale, including the inner scale (interface) and the outer scale (sharp-interface problem), then the two expansions are matched [26]. In this way, the calculation parameters in the PF equations and the physical qualities could be linked by:

$$d_0 = a_1 \frac{W}{\lambda} \quad (15)$$

$$\beta = a_1 \left[\frac{\tau}{\lambda W} - a_2 \frac{W}{D_L} \right] \quad (16)$$

In these equations, W and τ are the interface width and relaxation time, which are the length scale and time scale, respectively. $a_1=5\sqrt{2}/8$ and $a_2=47/75$, and $d_0=\Gamma/|m|(1-k)(c_\infty/k)$ is the chemical capillary length, where $\Gamma=\gamma_{sl}\Gamma_f/(\rho_s L_f)$ is the Gibbs-Thomson coefficient, γ_{sl} is S/L interface energy, T_f is the melting point of pure solvent and L_f is the latent heat, respectively. That is, [equation \(15\)](#) describes the Gibbs-Thomson effect, where λ is the coupling constant. [Equation \(16\)](#) contains two terms, where β is the kinetic coefficient. The first term describes the dissipation due to the homogeneous undercooling of the interface. The second term

represents the inhomogeneity of the temperature field inside the interface [46]. Due to the local equilibrium approximation, the kinetic undercooling is ignored in the simulation, i.e., $\beta=0$.

It should be noted, the governing [equation \(9\)](#) provides a clear connection between anisotropy of the microscopic and macroscopic levels [27,47]. Moreover, it unifies the anisotropy in equilibrium and non-equilibrium, revealing the interfacial anisotropy always plays an important role in solidification evolution.

2.3. Computational procedure

In the computation, the material parameters of Al-2.0wt.%Cu are shown in [Table 1](#) [48,49].

When solving [equations \(1\)-\(3\)](#) numerically, for a small time interval Δt , it is easy to show the relations in [equations \(17\)-\(18\)](#) [12], regarded as the initial conditions.

$$l \approx \left(\frac{8D_L \cdot \Delta t}{3} \right)^{1/2} \quad (17)$$

$$z_0 = z_\infty - V_p(t) \cdot \Delta t + \frac{V_p(t) \sqrt{2D_L}}{\sqrt{3} \cdot z_\infty (1-k)} (\Delta t)^{3/2} \quad (18)$$

When solving [equation \(5\)](#), the dispersion relation, the increase rate σ_ω satisfies [equation\(19\)](#) [12]:

$$\sigma_\omega = D_l (q_\omega^2 - \omega^2) - q_\omega V_l \quad (19)$$

Setting $\sigma_\omega=0$, the solution of [equation \(19\)](#) is:

$$q_\omega = \frac{V_l}{2D_l} + \sqrt{\omega^2 + \left(\frac{V_l}{2D_l} \right)^2} \quad (20)$$

Eliminating q_ω from these equations and inserting the values of z_0 and l , the time-dependent spectrum of the increase rate $\sigma_\omega(t)$ can be obtained. Taking $\sigma_\omega(t)$ to [equation \(6\)](#), the time-dependent amplitude can be obtained. In [equation \(6\)](#), $A_\omega(0)$ reflects the initial amplitude. Based on the approximation of the equilibrium fluctuation spectrum, $A_\omega(0)$ equals to the capillary length d_0 [42].

When solving the PF governing [equations \(9\)-\(10\)](#), the most important parameter is the interface width W [28]. The accuracy increases with the decrease of W , while the computational cost increases dramatically with the decrease of W . With the thin interface limitation, the magnitude of W just needs to be one order of magnitude smaller than the characteristic length scale of the structure [45,50]. The characteristic length of alloy solidification is $L_c \sim \sqrt{d_0 \cdot D_L / V_{tip}}$ [2], hence W was set to be $0.15 \mu\text{m}$. In the computation, the periodic boundary conditions were loaded for both the phase field and supersaturation field. The time step size was

chosen below the threshold of numerical instability for the diffusion equations, i.e., $\Delta t < (\Delta x)^2 / (4D_L)$. Finally, this paper used fixed grid size $\Delta x = 0.8W$ and time step size $\Delta t = 0.013\tau$.

Moreover, a fluctuating current J_U is introduced to the diffusion equation to consider the infinitesimal perturbation of thermal noise on the S/L interface. By using the Euler explicit time scheme:

$$U^{t+\Delta t} = U^t + \Delta t \left(\partial_t U - \vec{\nabla} \cdot \vec{J}_U \right) \quad (21)$$

The components of J_U are random variables obeying a Gaussian distribution, which has the maximum entropy relative to other probability distributions [40]:

$$\langle J_U^m(\vec{r}, \vec{t}) J_U^n(\vec{r}', \vec{t}') \rangle = 2D_L q(\psi) F_U^0 \delta_{mn} \delta(\vec{r} - \vec{r}') \delta(t - t') \quad (22)$$

In [equation \(22\)](#), the constant noise magnitude F_U^0 reflects the magnitude of F_U for a reference planar interface at temperature T_0 , defined as [39,51]:

$$F_U^0 = \frac{k\nu_0}{(1-k)^2 N_A c_\infty} \quad (23)$$

where ν_0 is the molar volume of the solute atom, and N_A is the Avogadro constant.

Finally, the program codes of the WL model and PF model were written by C++. The explicit Finite Difference Method (FDM) was used when solving the PF governing equations, and the Message Passing Interface (MPI) parallelization was adopted for improving the computational efficiency.

[Table 1. The material parameters of Al-2.0wt.%Cu for the simulation \[48,49\]](#)

Symbol	Value	Unit
Liquidus temperature, T_L	927.8	K
Solidus temperature, T_S	896.8	K
Diffusion coefficient in liquid phase, D_L	3.0×10^{-9}	m^2/s
Equilibrium partition coefficient, k	0.14	/
Alloy composition, c_∞	2.0	wt.%
Liquidus slope, m	-2.6	K/wt.%
Gibbs-Thomson coefficient, Γ	2.4×10^{-7}	K·m
Anisotropic strength of surface energy, ϵ_4	0.01	/

3. Results and discussion

In this section, dynamic solidification parameters are adopted in the simulations. The thermal gradient G is constant 100K/mm , while the pulling speed V_P increases from 0 to a fixed value $300\mu\text{m/s}$, for which the increase time is 0.5s , shown in Fig. 1(a). The intersection angle between the TGD and PCO of the crystal is 30° . The domain of the PF simulation is 2400×2400 grids, corresponding to $288.0\mu\text{m}\times 288.0\mu\text{m}$ in the real unit. It takes about 30 hours using 40 cores to finish one job.

3.1. The dynamic evolution in a dissipative system

Through exchanging heat and mass with the environment, solidification patterns are formed out of equilibrium, giving rise to dissipative structures [1,3]. Unlike equilibrium systems, the dissipative systems (non-equilibrium) develop patterns, structures, or behaviors that they do not have when first formed. Hence the dynamic evolution of the characteristic parameters with time should be described clearly to understand the dissipative structures better.

Fig. 1 shows the evolution of characteristic parameters, including the solute concentration ahead of the interface c_0 and the interface velocity V_I . In Fig. 1(a), the curves from the WL model and PF model show good consistencies before the crossover time ($t=0.67\text{s}$) of the planar instability, validating the accuracy of the PF model. After the crossover time, the curves from the WL model and PF model differ from each other. Because the parameters from the WL model are based on the planar interface, after the planar instability, the interfacial morphologies give rise to the differences between these two models. That is, the differences do not reflect the contradictions between these two models. Since the PF model can represent the interaction between the interfacial processes and transport processes, the following discussions of the evolution of the characteristic parameters at the interface are based on the PF simulations. In Fig. 1(a), at the initial stage, both c_0 and V_I increase. Then they reach the peaks and decrease. Through a period of oscillation, they turn into steady-state. The detailed evolution at each stage is following:

At the planar growth stage, in Fig. 1(a1), as solidification goes on, the interface velocity V_I increases. The accumulation of solute ahead of the S/L interface makes c_0 increases. At this stage, the evolution of c_0 and V_I can be directly identified by the sharp interface model (one-sided) of alloy solidification, expressed in equations (24)-(25). In the equations, ρ is the interface curvature, G is the thermal gradient, and \dot{T} is the cooling rate ($=G*V_P$), and $\partial_n c|^+$ is the gradient of solute concentration at the liquid side of the interface. Since $\partial_n c|^+ < 0$ in equations (25), to make the discussion intuitive, we set $|\partial_n c| = |\partial_n c|^+$.

$$c_0 = \frac{c_\infty}{k} - \frac{\rho \cdot \Gamma + G(z - V_I t)}{|m|} = \frac{c_\infty}{k} - \frac{\rho \cdot \Gamma + Gz + \dot{T}t}{|m|} \quad (24)$$

$$V_I = \left(-D_L \cdot \partial_n c \Big|_+ \right) / \left[(1-k)c_0 \right] = D_L \cdot |\partial_n c| / \left[(1-k)c_0 \right] \quad (25)$$

As time goes on, the planar instability occurs, represented by the sharp increment of the V_I curve in Fig. 1(a2). When the instability occurs, due to the conservation law at the interface, the solute concentration c_0 still increases after the crossover time. On the other hand, the cellular appear after the instability. Due to the curvature of the cellular, rather than diffusing only along the pulling direction of the planar interface, the solute can diffuse along multiple directions from the cellular tip to the liquid, resulting in the decrease of c_0 (see equation (24)). That is, after the planar instability, the solute concentration ahead of the interface first increases and then decreases, shown by the limited increment of the c_0 curve after the crossover time in Fig. 1(a2). As for the velocity V_I , equation (25) shows the competitive influences of $|\partial_n c|$ and c_0 depend on their specific values. Meanwhile, $|\partial_n c|$ is determined by V_I (by adjusting the diffusion length) and c_0 (by adjusting the difference between c_0 and c_∞), synergistically. It is evident that $|\partial_n c|$ has positive relations with both V_I and c_0 . After the planar instability, the increment of c_0 is very limited. By contrast, due to the increase of c_0 and the curvature of the cellular, the $|\partial_n c|$ increase greatly. As a result, the velocity V_I increases greatly, shown by the sharp increment of the V_I curve after the crossover time in Fig. 1(a2). After the peak of the c_0 curve, i.e., c_0 starts to decrease, the velocity V_I increase further (see equation (25)). As time goes on, the further decrease of c_0 means the difference between c_0 and c_∞ decreases, making $|\partial_n c|$ decrease. As a result, V_I reaches the maximum value and then decreases. With the decrease of V_I , the interface curvature ρ decreases, making c_0 increases (see equation (24)). The increase of c_0 brings the increase of $|\partial_n c|$, making the velocity V_I increase again. Then, the increase of V_I brings the increase of ρ , making c_0 decreases again. The cycle goes on and on till the steady-state stage, shown by the oscillating curves (from $t=1.0s$ to $t=2.2s$) in Fig. 1(a2).

As time goes further, solidification turns into the steady-state growth, shown by the stable curves (after $t=2.2s$) in Fig. 1(a3). At this stage, the dissipative structures achieve a quasi-steady state after a period of self-organization. Hence both c_0 and V_I turn into steady-state.

In conclusion, the consistencies at the planar stage between the WL model and PF model illustrate the accuracy of the PF simulations. After the planar instability, the interfacial effects make the evolution of the solute concentration c_0 and interface velocity V_I complex. Specifically, both c_0 and V_I reach the peaks successively, and then decrease. Subsequently, the c_0 curve and V_I curve show oscillatory behavior. Finally,

they turn into steady-state. The evolutionary characteristics of these parameters demonstrate the dissipation of solidification evolution.

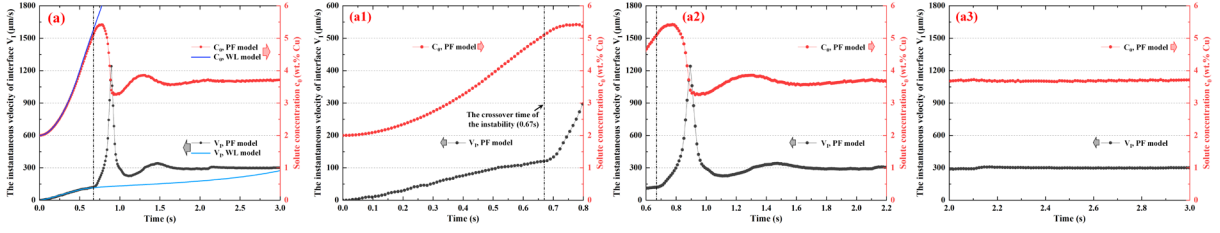


Fig. 1. The evolution of characteristic parameters: the solute concentration ahead of the interface c_0 and the instantaneous velocity of the interface V_I ; (a1), (a2), and (a3) are the enlarged versions of (a).

3.2. The role of solute diffusion in a dissipative system

On the one hand, the dynamic evolution of solidification shows dissipative features. On the other hand, the morphological evolution is determined by competitive influences of the interface curvature and velocity [27], depending strongly on the ratio τ/W^2 in the anisotropic PF model. According to the expression of the kinetic coefficient β in equation (16), one can obtain the relation ($\beta=0$):

$$\frac{\tau}{W^2} = a_2 \frac{\lambda}{D_L} \quad (26)$$

Combining equation (26) with equation (15), we can know that W , λ , a_1 , a_2 , and d_0 are constant in the PF simulation. The term $\tau/\lambda W$ represents the dissipation due to the undercooling of the interface, λ and W are constant, hence the magnitude of τ reflects the dissipation at the interface directly. Meanwhile, equation (26) illustrates the ratio τ/W^2 is determined by D_L . In conclusion, by adjusting the value of D_L , the dissipation of the interface can be altered, and the competitive effects of the interface curvature and velocity on the morphological evolution can be investigated.

In this section, different solute diffusion coefficients D_L are used in the PF simulations, where D_L are set to be 2.0×10^{-9} , 3.0×10^{-9} , 4.0×10^{-9} and 6.0×10^{-9} m^2/s , respectively. The evolution of the characteristic parameters with different D_L is shown in Fig. 2, including the solute concentration ahead of the interface c_0 and interface velocity V_I . On the one hand, the tendencies of c_0 and V_I curves show similar characteristics, including the sharp increment of the V_I curve, the peaks of the c_0 and V_I curves, and the oscillation of these curves. On the other hand, due to the different D_L , the degrees of dissipation at the interface are different in the evolution. Hence the quantitative characteristics of the evolution show differences, as following.

3.2.1. The planar growth and instability

At the planar growth stage, the accumulation of solute ahead of the S/L interface makes c_0 increases. The larger solute diffusion coefficient D_L corresponds to the lower degree of solute segregation, hence c_0 decreases from 2.0×10^{-9} to 6.0×10^{-9} at the same time between the simulations, shown in Fig. 2(a1). As for the velocity V_I , according to equation (25), V_I has positive relations with D_L , while it has a negative relation with c_0 . The larger D_L and smaller c_0 correspond to the larger V_I , i.e., V_I increases from 2.0×10^{-9} to 6.0×10^{-9} at the same time, shown in Fig. 2(b1).

As solidification goes on, the planar instability appears, represented by the sharp increment of the V_I curve in Fig. 2(b1)-(b2). To validate the PF results, the same parameters are used in the theoretical model. Specifically, by solving equations (4)-(6), the increase rates σ_ω and the perturbation amplitudes A_ω can be obtained, shown in Fig. 3. The time when σ_ω becomes positive, shown by the red curves in Fig. 3(a1)-(a4), representing the critical time of the marginal stability. It should be noted, the critical time t_c here just reflects the time that the perturbations can be amplified. At this moment, the perturbations at the interface are still infinitesimal, which cannot be observed at the mesoscale. Hence, rather than the time when σ_ω turns positive, we define the crossover time based on a specific value of A_ω . The time when the magnitude of A_ω reaches about $1 \mu\text{m}$ is identified as the crossover time of the planar instability, shown by the purple curves in Fig. 3(b1)-(b4). Finally, the crossover times from the theoretical model are 0.63s, 0.67s, 0.69s and 0.75s, in Fig. 3, consisting with those from the PF simulations, 0.65s, 0.67s, 0.69s, and 0.76s, shown in Fig. 2.

The consistency between the two different models validates the accuracy of the simulations. In Fig. 2, the crossover times of the planar instability increase from 2.0×10^{-9} to 6.0×10^{-9} . Moreover, the onset of the instability corresponds to different V_I , illustrating the interface velocity V_I is not the criterion of the instability. On the other hand, the onset of the instability corresponds to similar c_0 . Snapshots of the solute distribution at the onset time are shown in Fig. 4(a1)-(a4). The larger D_L means the larger diffusion length ahead of the interface. Meanwhile, the degrees of the solute segregation at the S/L interface are almost the same between the simulations with different D_L . The results demonstrate the conclusion that the excess free energy at the interface and corresponding interface energy are the critical parameters of the instability [52].

The detailed evolution of the interfacial morphologies with different D_L is shown Fig. 4(b1)-(b4), where the time differences between each two lines are the same. In Fig. 4(b1)-(b4), on the one hand, the amount of time of the Planar-Cellular-Transition (PCT) increases from 2.0×10^{-9} to 6.0×10^{-9} . On the other hand, the wave

number of the cellular decreases from 2.0×10^{-9} to 6.0×10^{-9} .

The phenomena can be explained by dissipation. Directional solidification is one kind of constrained growth process. To maintain the stable thermal gradient G and pulling speed V_P , the loaded parameters are dynamic but not static, i.e., the system we focus on is an open system [53]. By the exchange of heat and mass with the environment, solidification patterns are dissipative structures formed out of equilibrium. According to equation (26), the solute diffusion coefficient D_L has a negative relation with the relaxation time τ , as well as the degree of dissipation at the interface (determined by the ratio $\tau/\lambda W$). The smallest D_L corresponds to the largest τ , the maximum dissipation, and the largest degree of non-equilibrium. As a result, the amount of time of the PCT increases from 2.0×10^{-9} to 6.0×10^{-9} , shown in Fig. 4(b1)-(b4). Meanwhile, the solute at the S/L interface should satisfy the conservation law. After the planar instability, the solute still accumulates ahead of the interface till the appearing of the cellular. The longest time of the PCT means the longest time of the solute accumulation. Hence the peak of c_0 appears later and later from 2.0×10^{-9} to 6.0×10^{-9} , in Fig. 2(a2), and the value of the peak increases from 2.0×10^{-9} to 6.0×10^{-9} . As for the interface velocity V_I , the lower degree of non-equilibrium corresponds to the smaller V_I . In Fig. 2(b2), V_I decreases from 2.0×10^{-9} to 6.0×10^{-9} during the PCT stage. Meanwhile, the decreasing V_I makes the interface curvature ρ decrease from 2.0×10^{-9} to 6.0×10^{-9} . The larger ρ means the smaller wavelength and larger wave number, i.e., the wave number of the cellular decreases from 2.0×10^{-9} to 6.0×10^{-9} , shown in Fig. 4(b1)-(b4).

In conclusion, at the planar stage, the larger D_L corresponds to the larger V_I and smaller c_0 . Different V_I at the onset times of the planar instability illustrate that V_I is not the criterion of the instability. The decrease of the interface energy, induced by solute segregation at the S/L interface, can be regarded as the criterion of the instability. At the PCT stage, the larger D_L corresponds to the smaller τ , the less dissipation, and the smaller degree of non-equilibrium. As a result, the interface velocity V_I and interface curvature ρ decreases from 2.0×10^{-9} to 6.0×10^{-9} , while the amount of time of the PCT increases from 2.0×10^{-9} to 6.0×10^{-9} .

3.2.2. The dendrite growth

After the planar instability and the PCT stage, the dendrites (formed from the cellular) start to grow. At this stage, according to the rule of maximum surface energy, the crystal will seek to minimize the total energy by creating large curvature in the $\langle 100 \rangle$ direction, in Fig. 5(b1)-(b4). On the other hand, different values of D_L make the evolutionary characteristics differ from each other, including the solute concentration c_0 and interface velocity V_I , in Fig. 2(a2)-(b2), as well as the interfacial morphologies, shown in Fig. 5.

After the appearing of the cellular, c_0 starts to decrease. As mentioned before, the interface curvature ρ and velocity V_I decreases from 2.0×10^{-9} to 6.0×10^{-9} . Correspondingly, the gradient of solute concentration at the liquid side of the interface $|\partial_n c|$ decreases from 2.0×10^{-9} to 6.0×10^{-9} . Combined with [equation \(25\)](#), V_I increases further and reach its peak. The smallest D_L corresponds to the largest ρ , the lowest c_0 , and the largest $|\partial_n c|$. Hence the peak values of V_I decrease from 2.0×10^{-9} to 6.0×10^{-9} , shown [Fig. 2\(b2\)](#). Meanwhile, the larger interface velocity V_I gives rise to more sidebranches, shown in [Fig. 5 from \(b1\) to \(b4\)](#). It should be noted, the magnitude of D_L determines the diffusion length and the gradient of solute ahead of the interface, in [Fig. 5 from \(a1\) to \(a4\)](#). In addition to the coefficient D_L , the solute diffusion between the dendrite trunks is also influenced by the interface curvature, i.e., curvature-induced solute diffusion. During the directional solidification, due to the constrained growth conditions, the overall solute concentration is determined by the temperature. As a result, the distributions of solute field between the dendrite trunks show the same features, in [Fig. 5 from \(a1\) to \(a4\)](#), including the degree of solute segregation and the gradient.

In conclusion, the dendrites with smaller D_L grow out more sidebranches. On the other hand, although the solute diffusion coefficients D_L are different in the simulations, the distributions of solute field between the dendrite trunks show the same features, including the degree of solute segregation and the gradient.

3.2.3. The steady-state growth

As time goes on further, solidification turns into the steady-state growth, shown by the stable curves in [Fig. 2\(a3\)-\(b3\)](#) and the detailed evolution in [Fig. 6](#). At this stage, the dissipative solidification structures achieve a quasi-steady state after a period of self-organization. The overall propagation velocities of the S/L interface are the same in the simulations with different D_L , equaling to the pulling speed V_p . By contrast, due to the different D_L , the solute concentration ahead of the interface c_0 decreases from 2.0×10^{-9} to 6.0×10^{-9} , shown in [Fig. 2\(a3\)](#). As a result, the solute undercooling decrease from 2.0×10^{-9} to 6.0×10^{-9} , shown by the increasing distance between the dendrite tip and liquidus isothermal line from 2.0×10^{-9} to 6.0×10^{-9} in [Fig. 6 from \(a1\) to \(a4\)](#). On the other hand, differing from the solute field ahead of the S/L interface, under the constrained growth conditions of directional solidification, the overall solute concentration is determined by the temperature. The distributions of solute field between the dendrite trunks show the same features, in [Fig. 6 from \(a1\) to \(a4\)](#), including the degree of solute segregation and the gradient.

In addition, the primary dendrite arm space determines the shape of tip and the onset of sidebranches [54], in [Fig. 6](#), the space increases from 2.0×10^{-9} to 6.0×10^{-9} . This consists with the rule of length scale

selection in [equation \(27\)](#) [55], where σ^* is the selection constant, motivated by the value obtained for the minimum wavelength found in the stability analysis of planar growth. The larger D_L corresponds to the larger R_{tip} , as well as the larger dendrite arm space and the smaller number of primary dendrites.

$$R_{tip} = \frac{1}{\sigma^*} \sqrt{d_0 \frac{D_L}{V_I}} \quad (27)$$

As for the onset of sidebranches, comparing [Fig. 6\(b3\)](#) and [Fig. 6\(b4\)](#), with the same dendrite arm space and interface velocity, the dendrite with larger D_L grow out more sidebranches. This phenomenon consists with the previous conclusion. The larger D_L corresponds to larger degree of dissipation and non-equilibrium of the system. As a result, more non-equilibrium structures (sidebranches) grow out.

To represent this phenomenon more clearly, the simulations with a given number of dendrite are carried out. The evolution with different D_L and the same dendrite number at the steady-state stage is shown in [Fig. 7](#). Although they have the same interface velocity V_I and primary dendrite arm space λ_1 , the curvatures of the dendrite tip differ from each other, in [Fig. 7 from \(a1\) to \(a4\)](#), the curvature ρ decreases from 2.0×10^{-9} to 6.0×10^{-9} . In addition, with the same V_I and λ_1 , the characteristics of sidebranches also differ from each other, in [Fig. 7 from \(b1\) to \(b4\)](#), both the number and amplitude of the sidebranches decrease from 2.0×10^{-9} to 6.0×10^{-9} . The phenomena can also be explained by dissipation. The smaller D_L corresponds to the larger degree of dissipation and non-equilibrium of the system. As a result, the curvature ρ and the number and amplitude of the sidebranches decrease from 2.0×10^{-9} to 6.0×10^{-9} . The results illustrate that the evolution of interfacial morphologies does not has unique relationships with the characteristic parameters, such as V_I , c_0 , ρ and R_{tip} , etc. Because solidification patterns are dissipative structures formed out of equilibrium. The degree of dissipation and non-equilibrium of the system plays an important role in the evolution.

In conclusion, at the steady-state stage, the overall propagation velocities of the interface are the same in the simulations with different D_L and equal to V_p . On the other hand, although having the same interface velocity and primary dendrite arm space, the simulations with different D_L show different interface curvatures of the dendrite tip, as well as the number and amplitude of the sidebranches.

On the other hand, from the viewpoint of the whole domain, smaller D_L corresponds to higher degree of dissipation of the system, as well as more exchange of heat and mass with the environment. Hence more S/L interfaces are formed during solidification evolution. That is, the areas of the interfaces decrease from 2.0×10^{-9} to 6.0×10^{-9} , shown in [Fig. 4\(b1\)-\(b4\)](#), [Fig. 5\(b1\)-\(b4\)](#), [Fig. 6 \(b1\)-\(b4\)](#), and [Fig. 7 \(b1\)-\(b4\)](#).

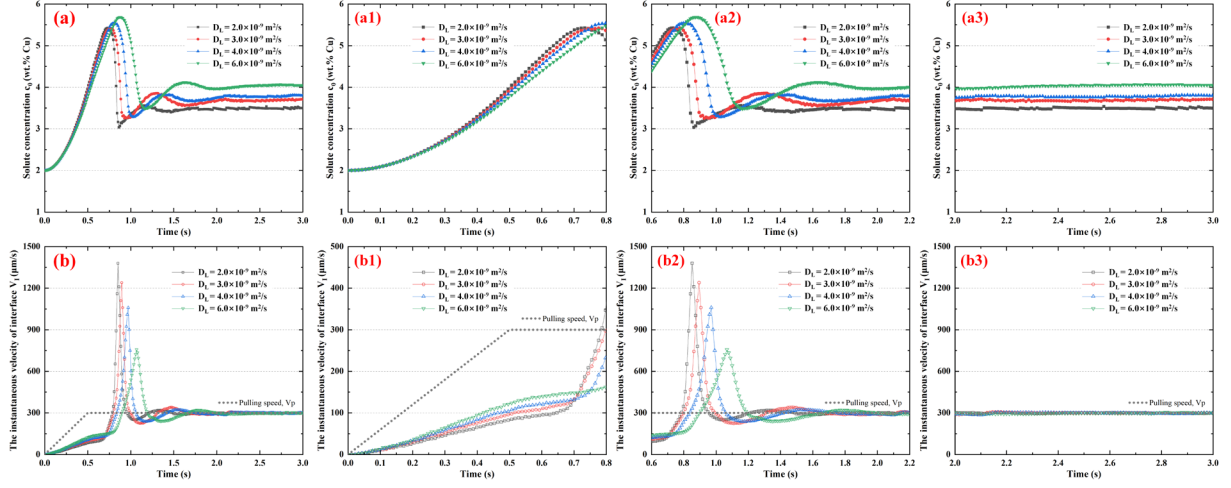


Fig. 2. The evolution of characteristic parameters with the different solute diffusion coefficients D_L : (a) the solute concentration c_0 and (b) the instantaneous velocity V_I ; (a1), (a2), and (a3) are the enlarged versions of (a); (b1), (b2), and (b3) are the enlarged versions of (b). (from the PF simulations)

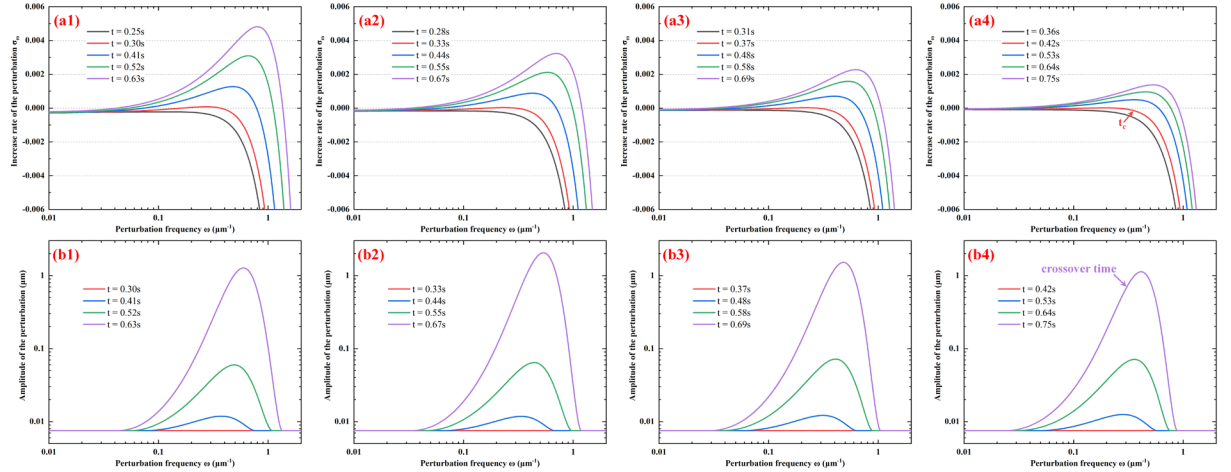


Fig. 3. Dynamic evolution of the instability predicted by the theoretical model with the different solute diffusion coefficients D_L : (a) The increase rate of the amplitude spectrum, (b) The evolution of the amplitude spectrum. (the diffusion coefficients are 2.0, 3.0, 4.0, and $6.0 \times 10^{-9} \text{ m}^2/\text{s}$, respectively)

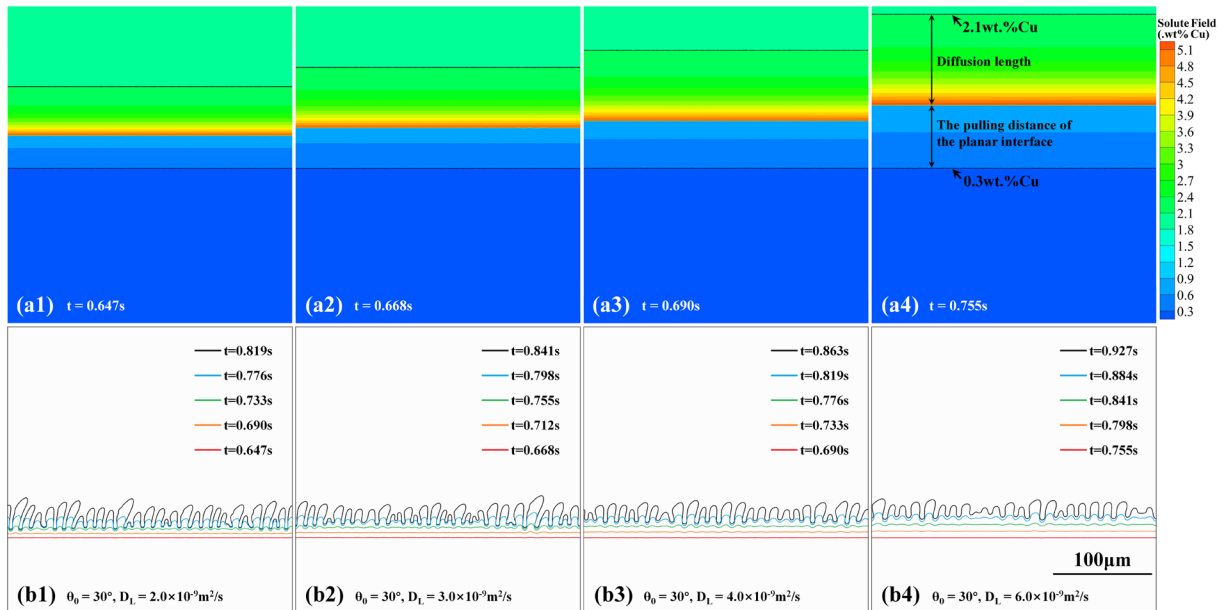


Fig. 4. (a) The interfacial morphology and solute field distribution with different solute diffusion coefficients D_L at the onset time of the planar instability; and (b) the corresponding evolution of interfacial morphologies with different D_L at the Planar-Cellular-Transition stage. (from the PF simulations)

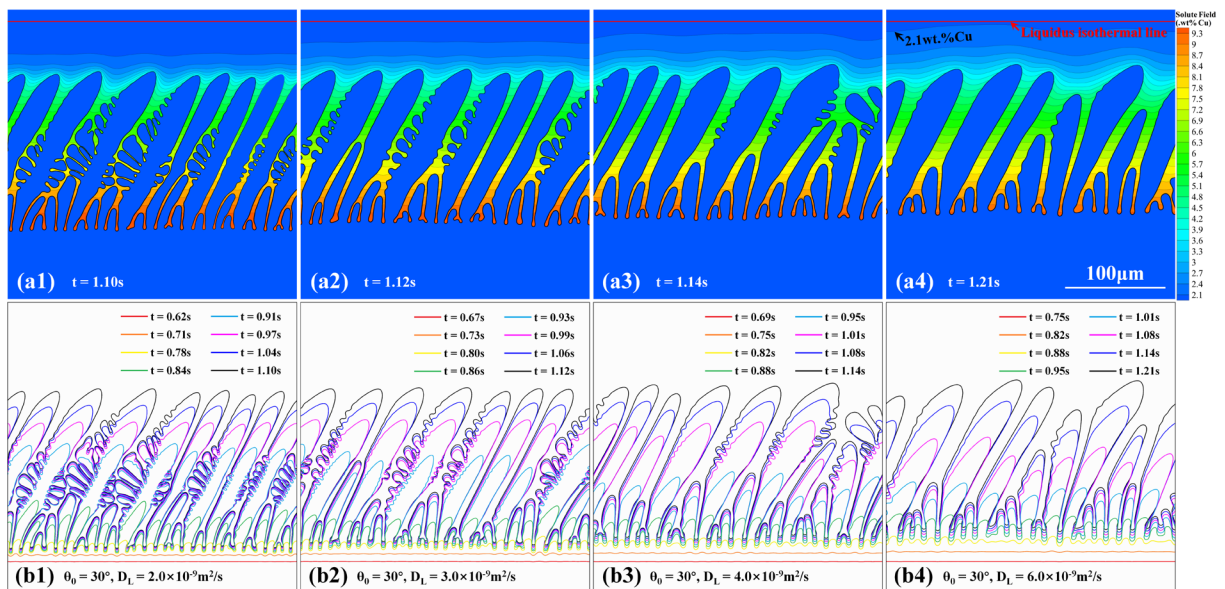


Fig. 5. (a) The interfacial morphology and solute field distribution with different solute diffusion coefficients D_L at the dendrite growth stage; and (b) the corresponding evolution of interfacial morphologies at this stage. (from the PF simulations)

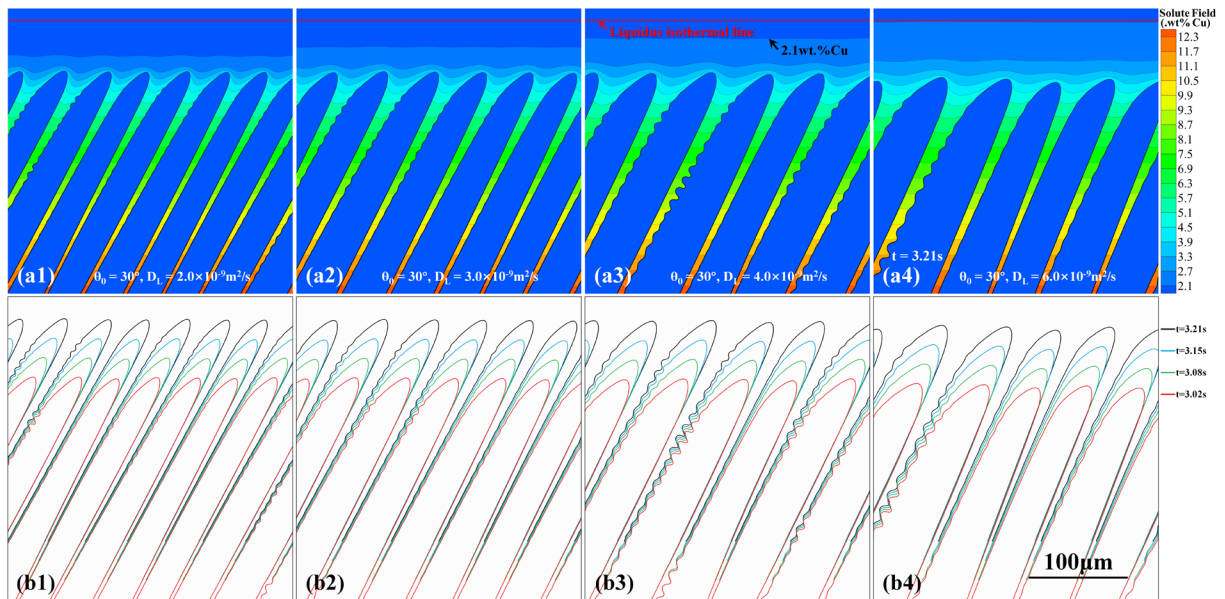


Fig. 6. (a) The interfacial morphology and solute field with different solute diffusion coefficients D_L at the steady-state stage ($t=3.21\text{s}$); and (b) the corresponding evolution of interfacial morphologies at this stage. (from the PF simulations)

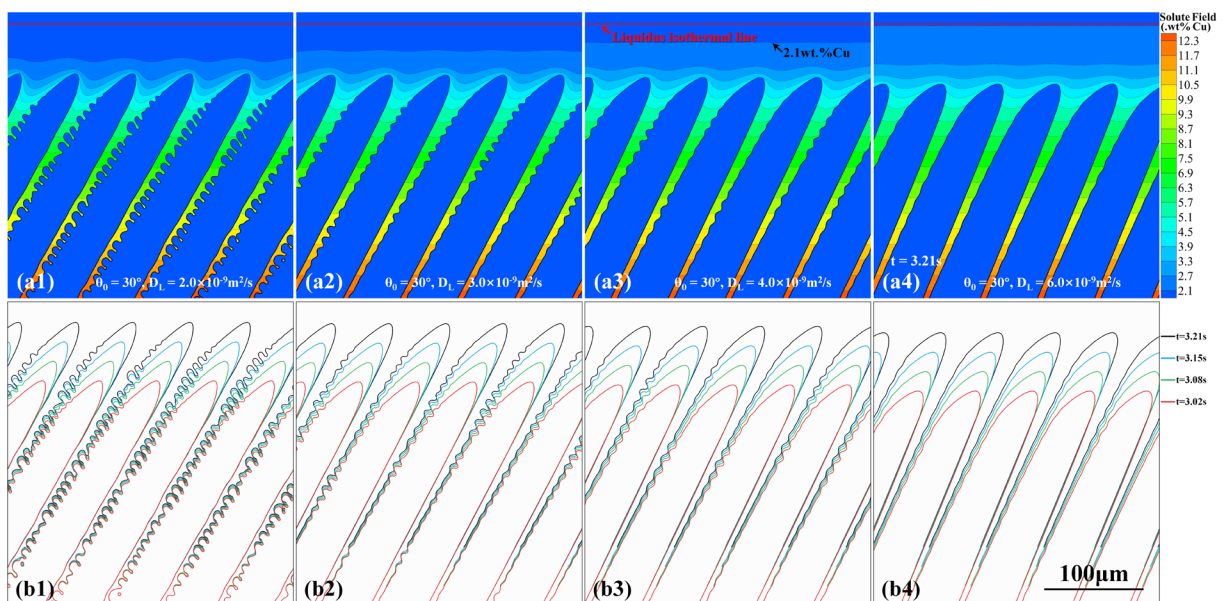


Fig. 7. (a) The interfacial morphology and solute field with the given number of dendrites and different solute diffusion coefficients D_L at the steady-state stage ($t=3.21\text{s}$); and (b) the corresponding evolution of interfacial morphologies at this stage. (from the PF simulations)

4. Conclusions

In this paper, the dynamic evolution during directional solidification is investigated via the quantitative PF model. Firstly, the evolution of the characteristic parameters with time is discussed in detail. Secondly, by adjusting the coefficient D_L , the dissipation due to an undercooling of the S/L interface can be altered. With different D_L , the dynamic evolution of the characteristic parameters and interfacial morphologies during the directional solidification is discussed, including the planar growth and instability, the dendrite growth, and the steady-state growth. The following conclusions can be drawn from the study:

(1) The consistencies at the planar stage between the WL model and PF model illustrate the accuracy of the PF simulations. After the planar instability, the interfacial effects make the evolution of the solute concentration c_0 and interface velocity V_I complex. Both c_0 and V_I reach the peaks successively, and then decrease. Subsequently, the c_0 curve and V_I curve show oscillatory behavior. Finally, they turn into steady-state. The evolutionary characteristics demonstrate the dissipation of solidification.

(2) At the planar stage, the larger D_L corresponds to the larger V_I and smaller c_0 . Different V_I at the onset times of the planar instability illustrate V_I is not the criterion of the instability. The decrease of the interface energy, induced by solute segregation at the S/L interface, can be regarded as the criterion of the instability. At the PCT stage, the larger D_L corresponds to the smaller τ , the less dissipation, and the smaller degree of non-equilibrium. Hence the interface velocity V_I and curvature ρ decreases from 2.0×10^{-9} to 6.0×10^{-9} , while the amount of time of the PCT increases from 2.0×10^{-9} to 6.0×10^{-9} .

(3) At the dendrite growth stage, the dendrites with smaller D_L grow out more sidebranches. On the other hand, although D_L are different in the simulations, the distributions of solute field between the dendrite trunks show the same features, including the degree of solute segregation and the gradient.

(4) At the steady-state stage, the overall propagation velocities of the interface are the same in the simulations with different D_L and equal to V_p . On the other hand, although having the same interface velocity and primary dendrite arm space, the simulations with different D_L show different interface curvatures of the dendrite tip, as well as the number and amplitude of the sidebranches.

(5) From the viewpoint of the whole domain, smaller D_L corresponds to higher degree of dissipation of the system, as well as more exchange of heat and mass with the environment. Hence more S/L interfaces are formed during solidification evolution. That is, the areas of the formed interfaces decrease from 2.0×10^{-9} to 6.0×10^{-9} , which can be found at each stage of directional solidification.

The investigations in this paper illustrate that the evolution of interfacial morphologies does not have unique relationships with the characteristic parameters, such as V_I , c_0 , ρ and R_{tip} , etc. Because solidification patterns are dissipative structures formed out of equilibrium. The degree of dissipation and non-equilibrium of the system plays an important role during the evolution, which should be considered in the study.

Reference

- [1] W. Kurz, D. J. Fisher, and R. Trivedi, *International Materials Reviews* **64**, 311 (2019).
- [2] J. A. Dantzig and M. Rappaz, *Solidification: 2nd Edition - Revised & Expanded* (EPFL Press, Lausanne, Switzerland, 2016).
- [3] W. Kurz, M. Rappaz, and R. Trivedi, *International Materials Reviews* **66**, 30 (2021).
- [4] C. Gu, Y. Lu, C. D. Ridgeway, E. Cinkilic, and A. A. Luo, *Scientific Reports* **9**, 13099 (2019).
- [5] Y. Wang, S. Li, Z. Liu, B. Yang, H. Zhong, and H. Xing, *Scripta Materialia* **186**, 121 (2020).
- [6] M. Rappaz, *Current Opinion in Solid State and Materials Science* **20**, 37 (2016).
- [7] M. Ohno, M. Yamashita, and K. Matsuura, *International Journal of Heat and Mass Transfer* **132**, 1004 (2019).
- [8] G. Azizi, S. Kavousi, and M. A. Zaeem, *Acta Materialia*, 117859 (2022).
- [9] W. A. Tiller, K. A. Jackson, J. W. Rutter, and B. Chalmers, *Acta Metallurgica* **1**, 428 (1953).
- [10] W. W. Mullins and R. F. Sekerka, *Journal of Applied Physics* **34**, 323 (1963).
- [11] W. W. Mullins and R. F. Sekerka, *Journal of Applied Physics* **35**, 444 (1964).
- [12] J. A. Warren and J. S. Langer, *Physical Review E* **47**, 2702 (1993).
- [13] Y. Chen, A.-A. Bogno, N. M. Xiao, B. Billia, X. H. Kang, H. Nguyen-Thi, X. H. Luo, and D. Z. Li, *Acta Materialia* **60**, 199 (2012).
- [14] W. Losert, B. Q. Shi, and H. Z. Cummins, *Proceedings of the National Academy of Sciences* **95**, 431 (1998).
- [15] A. Karma, in *Branching in nature*, edited by V. Fleury, J.-F. Gouyet, and M. Leonetti (Springer-Verlag, Heidelberg, 2001), pp. 365.
- [16] E. Brener, *Physical Review Letters* **71**, 3653 (1993).
- [17] R. Almgren, W.-S. Dai, and V. Hakim, *Physical Review Letters* **71**, 3461 (1993).
- [18] M. Ben Amar and E. Brener, *Physical Review Letters* **71**, 589 (1993).
- [19] A. Barbieri and J. S. Langer, *Physical Review A* **39**, 5314 (1989).
- [20] G. P. Ivantsov, *Dokl Akad Nauk SSSR* **58**, 567 (1947).
- [21] T. Takaki, M. Ohno, T. Shimokawabe, and T. Aoki, *Acta Materialia* **81**, 272 (2014).
- [22] M. A. Jaafar, D. R. Rousse, S. Gibout, and J.-P. Bédécarrats, *Renewable and Sustainable Energy Reviews* **74**, 1064 (2017).
- [23] M. Asta, C. Beckermann, A. Karma, W. Kurz, R. Napolitano, M. Plapp, G. Purdy, M. Rappaz, and R. Trivedi, *Acta Materialia* **57**, 941 (2009).
- [24] D. Tournet, H. Liu, and J. Llorca, *Progress in Materials Science* **123**, 100810 (2022).
- [25] L.-Q. Chen and Y. Zhao, *Progress in Materials Science* **124**, 100868 (2022).
- [26] M. Plapp, *Journal of the Indian Institute of Science* **96**, 179 (2016).
- [27] G. Caginalp, *Annals of Physics* **172**, 136 (1986).
- [28] A. Karma and W.-J. Rappel, *Physical Review E* **57**, 4323 (1998).
- [29] F. Yu and Y. Wei, *Metallurgical and Materials Transactions A* **49**, 3293 (2018).
- [30] Z. Dong, W. Zheng, Y. Wei, and K. Song, *Physical Review E* **89**, 062403 (2014).
- [31] H. Xing, K. Ankit, X. Dong, H. Chen, and K. Jin, *International Journal of Heat and Mass Transfer* **117**, 1107 (2018).
- [32] L. Wang, Y. Wei, J. Chen, and W. Zhao, *International Journal of Heat and Mass Transfer* **123**, 826 (2018).
- [33] Y. Song, S. Akamatsu, S. Bottin-Rousseau, and A. Karma, *Physical Review Materials* **2**, 053403 (2018).
- [34] D. Tournet and A. Karma, *Acta Materialia* **82**, 64 (2015).
- [35] J. Li, Z. Wang, Y. Wang, and J. Wang, *Acta Materialia* **60**, 1478 (2012).
- [36] P. Jiang, S. Gao, S. Geng, C. Han, and G. Mi, *International Journal of Heat and Mass Transfer* **161**, 120316 (2020).
- [37] A. Badillo and C. Beckermann, *Acta Materialia* **54**, 2015 (2006).
- [38] W. Zheng, Z. Dong, Y. Wei, and Y. Wang, *Crystal Research and Technology* **49**, 777 (2014).

- [39] B. Echebarria, A. Karma, and S. Gurevich, *Physical Review E* **81**, 021608 (2010).
- [40] A. Karma and W.-J. Rappel, *Physical Review E* **60**, 3614 (1999).
- [41] Z. Wang, J. Wang, and G. Yang, *Physical Review E* **80**, 052603 (2009).
- [42] Z. Wang, J. Wang, and G. Yang, *Applied Physics Letters* **94**, 061920 (2009).
- [43] A. Karma, *Physical Review Letters* **87**, 115701 (2001).
- [44] S. Gurevich, M. Amoozrezaei, and N. Provatas, *Physical Review E* **82**, 051606 (2010).
- [45] B. Echebarria, R. Folch, A. Karma, and M. Plapp, *Physical Review E* **70**, 061604 (2004).
- [46] M. Plapp, in *Handbook of Crystal Growth (Second Edition)*, edited by T. Nishinaga (Elsevier, Boston, 2015), pp. 631.
- [47] G. Caginalp, *Archive for Rational Mechanics and Analysis* **92**, 205 (1986).
- [48] A. J. Clarke, D. Tourret, Y. Song, S. D. Imhoff, P. J. Gibbs, J. W. Gibbs, K. Fezzaa, and A. Karma, *Acta Materialia* **129**, 203 (2017).
- [49] J. R. Morris, *Physical Review B* **66**, 144104 (2002).
- [50] H. Xing, X. Dong, H. Wu, G. Hao, J. Wang, C. Chen, and K. Jin, *Scientific Reports* **6**, 26625 (2016).
- [51] F. Yu, Y. Ji, Y. Wei, and L.-Q. Chen, *International Journal of Heat and Mass Transfer* **130**, 204 (2019).
- [52] F. Yu, arXiv preprint arXiv:2210.15123 (2022).
- [53] F. Yu, arXiv preprint arXiv:2210.15673 (2022).
- [54] H. Xing, X. L. Dong, C. L. Chen, J. Y. Wang, L. F. Du, and K. X. Jin, *International Journal of Heat and Mass Transfer* **90**, 911 (2015).
- [55] H. Müller-Krumbhaar and J. S. Langer, *Acta Metallurgica* **26**, 1697 (1978).